



# Solar hydrogen peroxide production on carbon nanotubes wired to titania nanorod arrays catalyzing As(III) oxidation

Seung Yo Choi<sup>a</sup>, Seonghun Kim<sup>a</sup>, Kyung Jin Lee<sup>b</sup>, Jin Young Kim<sup>b</sup>, Dong Suk Han<sup>c</sup>, Hyunwoong Park<sup>a,\*</sup>

<sup>a</sup> School of Energy Engineering, Kyungpook National University, Daegu 41566, Republic of Korea

<sup>b</sup> Fuel Cell Research Center, Korea Institute of Science and Technology, Seoul 02792, Republic of Korea

<sup>c</sup> Center for Advanced Materials (CAM), Qatar University, Doha 2713, Qatar

## ARTICLE INFO

### Keywords:

Artificial photosynthesis  
Oxygen reduction reaction  
Arsenic oxidation  
Carbon electrode  
TiO<sub>2</sub> nanorod arrays

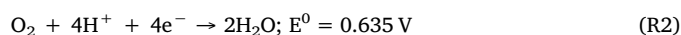
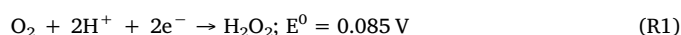
## ABSTRACT

We present an off-grid, standalone electrocatalytic H<sub>2</sub>O<sub>2</sub> production reaction (HPR) using carbon nanotubes (CNT) wired to hydrogen-treated TiO<sub>2</sub> nanorod (h-TNR) arrays catalyzing the oxidation of As(III) to As(V) under simulated solar light (AM 1.5; 100 mW cm<sup>-2</sup>). Loading CNT onto acid-treated carbon paper (a-CP) significantly enhances the catalytic 2-electron transfer to O<sub>2</sub>, leading to a Faradaic efficiency (FE) of ~100% for the HPR. To drive the HPR, the 2-electron oxidation of toxic As(III) to less toxic As(V) that accompanies the production of the proton/electron couples is achieved at an FE of > 80% using the h-TNR arrays. The high FEs of the anodic and cathodic reactions are maintained over 10 h when a direct-current voltage of 0.7 V is applied to the h-TNR photoanode and CNT/a-CP cathode pair. The coupling of a mono-Si photovoltaic array that is one-tenth the size of h-TNR photoanode to the pair of h-TNR and CNT/a-CP successfully drives the standalone operation of both reactions at the high FEs (> 90%). The surface characterization of the as-synthesized materials and the reaction mechanism are discussed in detail.

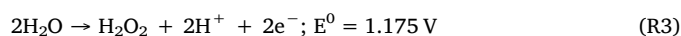
## 1. Introduction

Hydrogen peroxide (H<sub>2</sub>O<sub>2</sub>) is widely used as an eco-friendly bleaching oxidant in pulps and papers (48% in global market), textiles (16%), wastewater (11%), and other materials, including food and personal care products (25%) [1]. While its global market size was close to USD 4 billion in 2015, it is projected to grow > 5% yearly, reaching approximately USD 6.4 billion (> 5.7 million metric tons [2]) by 2024. Industrially, over 95% of H<sub>2</sub>O<sub>2</sub> is produced via the sequential hydrogenation and oxidation of alkyl anthraquinone [1,3,4]; however, this process suffers from multiple inefficient synthesis steps and a significant quantity of byproducts [5].

Alternative H<sub>2</sub>O<sub>2</sub> production technologies have emerged, among which electrocatalytic synthesis via the reduction of molecular O<sub>2</sub> (R1) has received growing attention because of the inexpensive and easy installation, absence of toxic byproducts, connectivity with other valuable processes, and extensibility to the utilization of renewable energy. The H<sub>2</sub>O<sub>2</sub> production reaction (HPR) with 2-electron (2e<sup>-</sup>) transfer usually competes against the conventional oxygen reduction reaction (ORR) with 4-electron transfer (R2) and is kinetically faster than the latter [6,7].



Potential values for R1–R3 are with respect to saturated calomel electrode (SCE) at pH of 6. HPR can occur via the water oxidative pathway (R3); yet unavoidable post-oxidation occurs at lower potentials (i.e., reversed R1), reducing the efficiency.



On the other hand, the reductive HPR (R1) requires less potential than other competitive 2e<sup>-</sup> reactions (e.g., hydrogen evolution reaction (HER)) in aqueous media. This suggests that a well-designed electrochemical system ensures a high-efficiency HPR by minimizing undesired side (sequential and/or parallel) reactions [8].

To reduce the electrical energy input while using sunlight, several photosystems with suspension-type photocatalytic and film-type photoelectrochemical (PEC) reactions have been designed [9–11]. The former typically showed low efficiencies for HPR due to the inevitable decomposition pathways without post-separation of the produced H<sub>2</sub>O<sub>2</sub> [12,13]. On the other hand, the PEC process with the configuration of

\* Corresponding author.

E-mail address: [hwp@knu.ac.kr](mailto:hwp@knu.ac.kr) (H. Park).

<https://doi.org/10.1016/j.apcatb.2019.03.060>

Received 19 September 2018; Received in revised form 19 March 2019; Accepted 21 March 2019

Available online 30 March 2019

0926-3373/ © 2019 Elsevier B.V. All rights reserved.

photoanodes and cathodes for water oxidation (reversed R2) and HPR, respectively, exhibited relatively high Faradaic efficiencies (FEs) ( $\sim 80\%$ ). However, this was mostly based on the half-reaction (R1 or R3) performance of the employed photoanode or cathode, whereas the device-based efficiency was poor using electron-donating chemicals [14,15].

Herein, we attempted to develop high-efficiency, robust carbon materials for the electrocatalytic HPR and coupled the HPR with PEC processes to realize sunlight-driven  $\text{H}_2\text{O}_2$  production. Carbon-based electrodes have been widely employed to accelerate interfacial electron transfer to  $\text{O}_2$  [16–19]. The optimal Faradaic efficiency of HPR with carbon materials was reported to vary between 60 and  $\sim 100\%$  [20], depending on their surface states, applied powers, electrolytes, and reactor configuration. In this study, fibered carbon paper (CP) electrodes were modified with carbon nanotubes (CNT) to enhance the catalytic 2e-transfer reactions and improve the mass transfer of  $\text{O}_2$  bubbles, leading to an outstanding Faradaic efficiency of  $\sim 100\%$ . Then, the CNT electrode was coupled to sunlit  $\text{TiO}_2$  nanorod (TNR) and hydrogen-treated TNR (h-TNR) arrays that drive the oxidation of As(III) to less toxic As(V) instead of the oxygen evolution reaction (OER). The hydrogen treatment of TNR is effective for creating oxygen vacancies [21,22], thereby improving the electrical conductivity and oxidative photocurrents for As(III) that is a critical water contaminant [23]. Finally, photovoltaic (PV)-coupled PEC hybrid reactions have been designed to demonstrate an off-grid, standalone process (Fig. 1).

## 2. Experimental

### 2.1. Synthesis of materials

Carbon papers (TGP-H-060, Toray Co.,  $1\text{ cm} \times 1\text{ cm}$ ) were treated with aqua regia for 1 h, rinsed with deionized water ( $> 18\text{ M}\Omega\text{ cm}$ , Barnstead), and dried in an  $\text{N}_2$  stream. Virgin and acid-treated carbon papers (CP and a-CP, respectively) were loaded with carbon nanotubes (CNT, CM-100, Hanwha Nanotech Corp., pore size of 10–15 nm) via a vacuum filtration and drying process [24,25]. A mixture of CNT (0.1 g), polytetrafluoroethylene (1 mL, 60 wt% dispersion in  $\text{H}_2\text{O}$ , Sigma-Aldrich), and 1-butanol (1 mL,  $> 99\%$ , Sigma-Aldrich) in deionized water (50 mL) was prepared. After stirring for 1 h, the mixture was sonicated in an ultrasonic bath for 90 min [26]. Next, 1 mL of the mixture was dropped onto CP and a-CP and passed through them using a vacuum pump. Then, the samples loaded with CNT (CNT/CP and CNT/a-CP) were dried at  $50^\circ\text{C}$  for 1 h. This process was repeated until their overall weight increased by 30%. Finally, the samples were annealed at  $300^\circ\text{C}$

for 1 h to remove organic chemicals. The morphologies of the carbon samples were analyzed using field-emission scanning electron microscopy (FE-SEM, Hitachi S4800).  $\text{TiO}_2$  nanorod (TNR) arrays were synthesized on the fluorine-doped  $\text{SnO}_2$  layer ( $\sim 500\text{ nm}$ , FTO, Pilkington)-coated soda lime glass via hydrothermal treatment for 5 h and annealing at  $450^\circ\text{C}$  for 30 min. The as-synthesized TNRs were further treated at  $350^\circ\text{C}$  for 2 h in an  $\text{H}_2/\text{Ar}$  stream ( $\text{H}_2:\text{Ar} = 5:95$ ) at 1 bar, yielding h-TNR. The synthesis method is presented in detail elsewhere [22].

### 2.2. Electrochemical measurements and product analysis

The as-synthesized carbon samples (CP, a-CP, CNT/CP, and CNT/a-CP; working electrodes), a saturated calomel electrode (SCE, reference electrode), and a Pt plate (counter electrode) were placed in a customized glass reactor containing aqueous sodium sulfate ( $0.1\text{ M Na}_2\text{SO}_4$ , Daejung). If necessary, two-compartment reactors separated by a proton-exchange membrane (PEM, Nafion 117, Chemours) were employed, where the working and reference electrodes were placed in the same compartment, while the counter electrode was located in the other compartment. In both the undivided and divided reactors,  $\text{O}_2$  was bubbled through the solution with the working electrode for 1 h prior to electrochemical analysis using a potentiostat/galvanostat (CompacStat, Ivium). Linear sweep voltammograms (LSVs) were obtained via a potential sweep from  $+1.6$  to  $-2.4\text{ V}$  vs. SCE at a scan rate of  $5\text{ mV s}^{-1}$ . In bulk electrolysis for  $\text{H}_2\text{O}_2$  production, constant potentials ( $-0.33$ ,  $-0.53$ , and  $-0.63\text{ V}$  vs. SCE) or constant currents were applied to the samples. During the electrolysis, aliquots were intermittently sampled and analyzed via a well-known DMP method for  $\text{H}_2\text{O}_2$  [27]. For the quantification of the produced  $\text{H}_2\text{O}_2$ , a standard curve fit ( $r^2 > 0.99$ ) between known concentrations of  $\text{H}_2\text{O}_2$  (28%, Duksan) and corresponding spectral absorbance values at  $\lambda = 454\text{ nm}$  was established using ultraviolet (UV)–visible spectroscopy (UV-2450, Shimadzu).

To examine the electron-transfer kinetics and selectivity, rotating ring disk electrode (RRDE, geometric area  $0.247\text{ cm}^2$ ) voltammetry was performed using an AFMSRCE advanced electrochemical system (Pine Instrument Co., USA). A glassy carbon electrode for the catalyst ink was used as a working electrode, while SCE and Pt were used as the reference and counter electrodes, respectively. The carbon samples were crushed and mixed with  $50\text{ }\mu\text{L}$  of Nafion, which was dropped in isopropanol ( $500\text{ }\mu\text{L}$ ) and sonicated for 1 h. Then,  $3\text{ }\mu\text{L}$  of the ink was dispersed onto a rotating glassy carbon electrode. Prior to the RRDE voltammetry, the electrolyte ( $0.1\text{ M Na}_2\text{SO}_4$ ) was purged with  $\text{O}_2$ . The potential was cathodically scanned from  $0.43$  to  $-0.53\text{ V}$  vs. SCE at a scan rate of  $5\text{ mV s}^{-1}$ . The electron transfer number and  $\text{H}_2\text{O}_2$  selectivity were estimated using the equations presented in the Supporting Information [28,29].

The photoelectrochemical (PEC) behaviors of TNR and h-TNR in aqueous sodium sulfate solution ( $0.1\text{ M}$ ) were examined via a potential sweep from  $-0.8$  to  $0.9\text{ V}$  vs. SCE at a scan rate of  $5\text{ mV s}^{-1}$  under simulated solar light ( $100\text{ mW cm}^{-2}$ ) from a 150-W Xe arc lamp (ABET Technology) equipped with an air mass (AM) 1.5 filter. For the PEC bulk oxidation of As(III), constant potentials ( $0.5$  and  $0.8\text{ V}$  vs. SCE) or a constant current ( $1\text{ mA cm}^{-2}$ ) were applied to the TNR and h-TNR electrodes in an aqueous sulfate solution ( $0.1\text{ M}$ ) with  $1\text{ mM}$  As(III) ( $\text{NaAsO}_2$ , Sigma-Aldrich,  $\geq 90\%$ ) while irradiating the simulated sunlight. The As(V) that was produced by the oxidation of As(III) was quantified using a colorimetric method reported elsewhere [30,31].

For the dual reaction (i.e.,  $\text{H}_2\text{O}_2$  production and As(III) oxidation), CNT/a-CP and h-TNR (or TNR) electrode pairs were placed in a two-compartment reactor separated by a PEM (Nafion 117, Chemours). A direct-current (DC) voltage of  $0.7\text{ V}$  ( $0.7\text{ V}_{\text{DC}}$ ) was applied to the irradiated h-TNR (anode) with respect to CNT/a-CP (cathode) in aqueous sodium sulfate ( $0.1\text{ M}$ ) using a DC power supply (E3647A, Keysight Technologies), while  $\text{O}_2$  was continuously purged through the catholyte. During the electrolysis, the photocurrent ( $I_{\text{ph}}$ ) was recorded, and

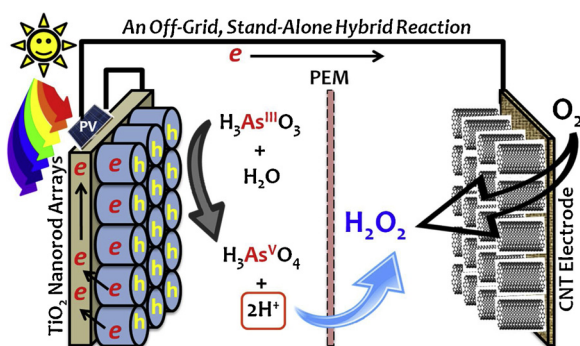


**Fig. 1.** Schematic illustration of as-designed stand-alone PV-PEC hybrid devices for the oxidation of toxic As(III) to less toxic As(V) oxidation and the reduction of  $\text{O}_2$  to  $\text{H}_2\text{O}_2$  at hydrogen-treated  $\text{TiO}_2$  nanorod (h-TNR) array and carbon nanotubes (CNT) electrodes, respectively. The coupling of a mono-Si photovoltaic array that is one-tenth the size of h-TNR photoanode to the pair of h-TNR and CNT successfully drives the standalone operation of both reactions at the high FEs ( $> 90\%$ ), a solar-to- $\text{H}_2\text{O}_2$  conversion energy efficiency of  $\sim 1\%$ , which is close to the efficiency upper limit of the  $\text{TiO}_2$  photoanode.

the aliquots in the anolyte and catholyte were sampled and quantified. The Faradaic efficiencies (FE) for  $\text{H}_2\text{O}_2$  and As(V) were estimated using the following equation:

$$\text{FE} (\%) = P (\text{mol}) \times 2F / (I \times t) \times 100\%$$

where  $P$ ,  $F$ ,  $I$ , and  $t$  refer to the products ( $\text{H}_2\text{O}_2$  or As(V)), the Faradaic constant ( $96,485 \text{ C mol}^{-1}$ ), the current ( $\text{C s}^{-1}$ ), and time (s), respectively. Finally, a commercial monocrystalline Si PV cell (Toyscience) was directly coupled to the h-TNR and CNT/a-CP pair in the divided reactor, while each biased (half) potential of the pair was recorded with respect to the SCE. The solar-to- $\text{H}_2\text{O}_2$  conversion energy efficiency was estimated using the following equation:

$$\text{Efficiency} = (\text{Productionrate} \times \Delta G_f^\circ \times 100\%) / (P \times A)$$

where  $P$  is the power of incident light ( $100 \text{ mW cm}^{-2}$ ),  $\Delta G_f^\circ$  is the Gibbs free energy for formation of  $\text{H}_2\text{O}_2$  ( $120.35 \text{ kJ mol}^{-1}$ ), and  $A$  is area ( $\text{cm}^2$ ). Throughout the text, unless otherwise specified, the unit for the electrochemical potential is simply expressed as V (without “vs. SCE”), for simplicity.

### 3. Results and discussion

#### 3.1. Hydrogen peroxide production using carbon electrodes

The acid-treated carbon paper samples (a-CP) were composed of  $\sim 190\text{-}\mu\text{m}$ -thick fibers, which were packed in the form of a mat (Fig. 2a). The overall morphology of the a-CP was similar to that of virgin carbon paper (CP, see Fig. S1), whereas the a-CP surface was clean, without any “carbon feathers.” In the CNT/a-CP sample, the top of the a-CP was covered with particle-agglomerate-like layer which was

composed of CNT having a tube thickness of  $< 50 \text{ nm}$ . The cross-sectional image confirms the two-layer configuration with the underlying a-CP and overlying CNT. CNT/CP has a similar morphology (Fig. S1). This double-layer configuration appears to be beneficial for the gas transfer through the porous carbon substrates and the subsequent electrochemical reaction at the gas/liquid interface.

The electrochemical behavior of bare and modified carbon electrodes was examined in an aqueous solution of sodium sulfate ( $0.1 \text{ M}$ ) purged with  $\text{O}_2$  (Fig. 2b). The CP electrode showed an onset potential ( $E_{\text{on}}$ ) of  $-0.28 \text{ V}$ , and the increase in the current with an increasing potential was not large (e.g.,  $\sim 6.7 \text{ mA cm}^{-2} \text{ V}^{-1}$ ). Although acid treatment was reported to increase the electrical conductivity of carbon electrodes [24,32], its effect on  $E_{\text{on}}$  and  $I$  was not significant in this study (Fig. S2). However, when CNTs were embedded into the CP,  $E_{\text{on}}$  was shifted by approximately  $0.17 \text{ V}$ ; more significantly,  $I$  increased significantly (by a factor of 2.5) with the increase of  $E$  without any sign of a mass-transfer limit (i.e., limiting current). The overall electrochemical behavior of CNT/a-CP was similar to that of CNT/CP;  $E_{\text{on}}$  was slightly shifted to the positive direction, and  $\Delta I$  was comparable.  $\text{N}_2$ -purging significantly shifted  $E_{\text{on}}$  to approximately  $-1.3 \text{ V}$  with a steeper  $\Delta I$ , which is attributed to the HER with  $2e$  transfer.

The heterogeneous electrocatalytic electron transfers were further examined using RRDE voltammetry (Fig. 2c–e). Regardless of the type of carbon samples, the ring currents ( $I_r$ ) attributed to the  $\text{H}_2\text{O}_2$  oxidation were significantly lower than the disc currents ( $I_d$ ) attributed to the  $\text{H}_2\text{O}_2$  production. This difference is usually observed for highly porous carbon electrodes with a non-uniform film thickness [33], owing to localized turbulence flows. Nevertheless, redox current peaks at  $E = -0.1 \text{ V}$  were observed for all samples, the potential of which was close to the electrochemical potential of the ORR with  $2e$  transfer (R1).

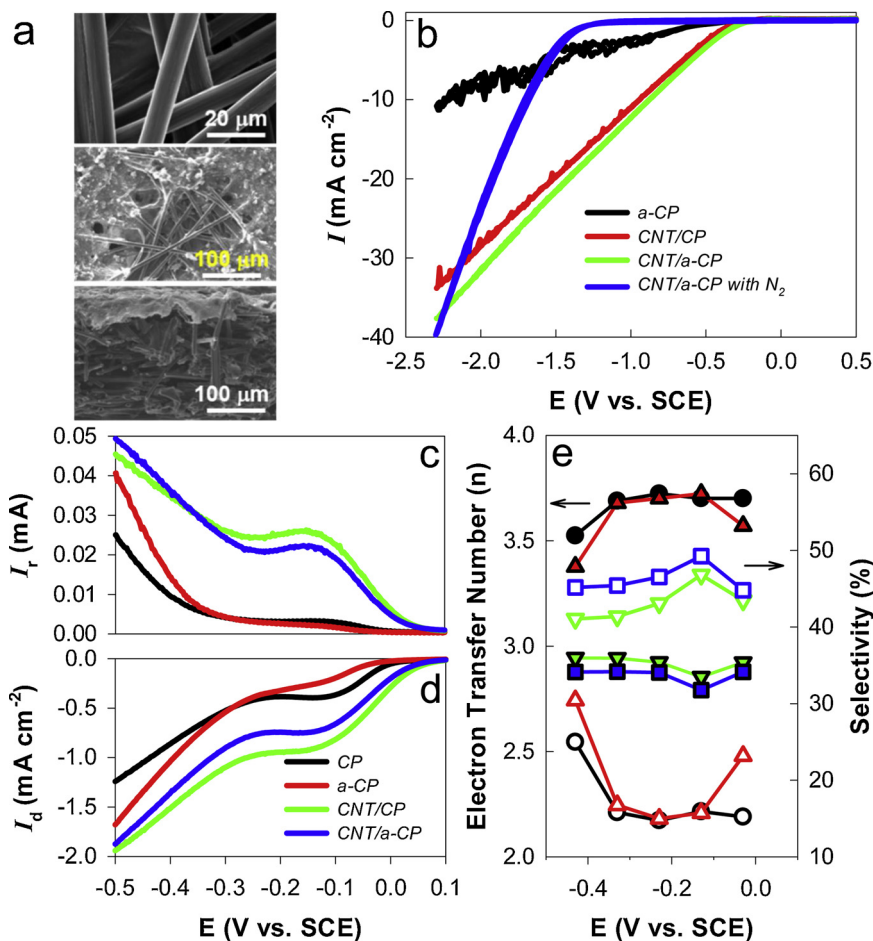


**Fig. 2.** (a) SEM images of acid-treated carbon papers (a-CP; top panel) and CNT-loaded a-CP (CNT/a-CP; middle and bottom panels: top and cross-sectional views, respectively). (b) Cyclic voltammograms of bare (CP and a-CP) and CNT-loaded (CNT/CP and CNT/a-CP) electrodes under continuous  $\text{O}_2$  or  $\text{N}_2$  purging through an aqueous solution of sodium sulfate ( $0.1 \text{ M}$ ). (c, d) Ring and disk current ( $I_r$  and  $I_d$ , respectively) profiles of the carbon electrodes under  $\text{O}_2$  purging through an aqueous solution of sodium sulfate ( $0.1 \text{ M}$ ). (e) Electron transfer number and  $\text{H}_2\text{O}_2$  selectivity estimated from Fig. 2c and d. See the Supporting Information for the equations. The solid and open symbols represent the electron transfer number and selectivity, respectively. The circles, normal triangles, reverse triangles, and squares represent CP, a-CP, CNT/CP, and CNT/a-CP, respectively.

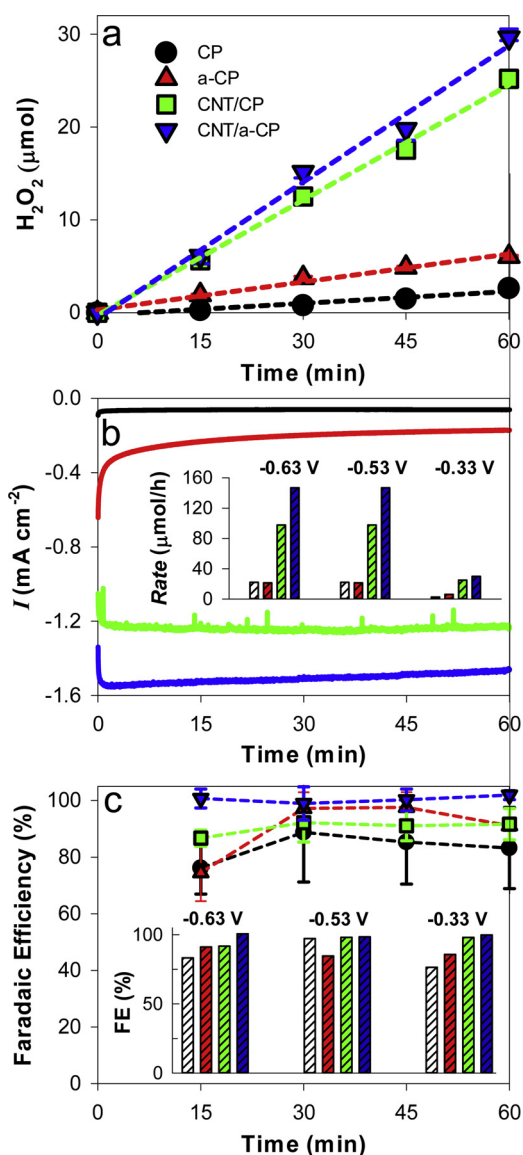


**Fig. 3.** Electrochemical  $\text{H}_2\text{O}_2$  production using carbon electrodes held at  $-0.33$  V vs. SCE in aqueous sodium sulfate ( $0.1$  M) purged with  $\text{O}_2$ . (a) Time-profiled  $\text{H}_2\text{O}_2$  production, (b) current changes (from top: CP, a-CP, CNT/CP, and CNT/a-CP), and (c) Faradaic efficiencies (FEs; see Fig. 3a for symbols). The insets in (b) and (c) show the  $\text{H}_2\text{O}_2$  production rates and FEs, respectively, using carbon electrodes (from left: CP, a-CP, CNT/CP, and CNT/a-CP) with respect to the applied potential ( $-0.66$ ,  $-0.53$ , and  $-0.33$  V vs. SCE).

During the ORR, the electron transfer numbers of the CP and CNT/CP samples were  $\sim 3.7$  and  $\sim 2.9$ , respectively, and their  $\text{H}_2\text{O}_2$  selectivity was estimated to be  $\sim 15\%$  and  $\sim 40\%$ , respectively. Considering the non-ideal conditions for RRDE voltammetry (porous electrode structure, distance between the ring and disc, loading amount of carbons, etc.), the difference between CP and CNT/CP (rather than the observed figures themselves) is meaningful. Obviously, loading CNT into the CP reduced the electron transfer number to  $\sim 2$ , thereby enhancing the  $\text{H}_2\text{O}_2$  selectivity by a factor of  $> 2$ . A similar enhancement was observed with the loading of CNT into a-CP. Although the CP and a-CP can drive the HPR, their primary role appears to be supporting the CNT while proving porosity for effective  $\text{O}_2$  diffusion, whereas the CNT should play a catalytic role in the HPR.

Fig. 3 shows the bulk electrolysis using carbon electrodes held at various potentials ( $-0.63$ ,  $-0.53$ , and  $-0.33$  V) in aqueous sodium sulfate solutions ( $0.1$  M, pH  $\sim 6$ ) under  $\text{O}_2$  purging. At  $-0.63$  V,  $\text{H}_2\text{O}_2$

was linearly produced during the electrolysis with all carbon electrodes; CP and a-CP showed similar electrocatalytic activity for  $\text{H}_2\text{O}_2$  production (Fig. 3a). This similarity was found at the other potentials (Fig. S3). On the other hand, CNT/CP and CNT/a-CP showed remarkably enhanced the  $\text{H}_2\text{O}_2$  production rates ( $\sim 130$  and  $200 \mu\text{mol h}^{-1} \text{cm}^{-2}$  for  $I$  of  $\sim 7.3$  and  $8.5 \text{ mA cm}^{-2}$  at  $E = -0.63$  V, respectively; see Fig. S4), which were  $\sim 5$  and  $8$  times higher, respectively, than those without CNT. The electrocatalytic activities were also enhanced by loading CNT at the other potentials ( $E = -0.53$  and  $-0.33$  V), where the HPR rates increased by  $4$ – $5$  times (Fig. 3b inset). The increased  $\text{H}_2\text{O}_2$  production with CNT loading is attributed to the increase of  $I$ ; CNT/a-CP generated the largest  $I$ , followed by CNT/CP, a-CP, and CP (Fig. 3b). With  $\text{N}_2$  purging,  $I$  was nearly zero (max  $\sim 0.1 \text{ mA cm}^{-2}$ ), and no  $\text{H}_2\text{O}_2$  was produced, regardless of  $E$  (Fig. S5). To compare the intrinsic electrocatalytic activities of carbon electrodes without the contribution of  $I$ , the Faradaic efficiency (FE) for HPR was estimated (Fig. 3c). The CP electrode showed a nearly invariable FE of  $\sim 76\%$  during the electrolysis period, which was enhanced to  $\sim 82$ ,  $85$ , and  $100\%$  with a-CP, CNT/CP, and CNT/a-CP, respectively. Similar tendencies were observed at other potentials (Fig. 3c inset). For further comparison, a constant value of  $I$  (i.e.,  $1 \text{ mA cm}^{-2}$ ) was applied to carbon electrodes, and the FE values were estimated. Similar to the potentiostatic condition, CNT loading enhanced the FE ( $\sim 100\%$ ) (Fig. S6). These results obviously show the positive effects of acid treatment and CNT loading; the former removes surface carbons (e.g., dangling carbons) and enhances the electrical conductivity, and the latter not only enhances the electrical conductivity but also creates a more porous structure, accelerating the solid/liquid/gas interfacial reaction.

### 3.2. Photoelectrochemical arsenite oxidation using thermochemically reduced TNR arrays

To drive the HPR using sunlight,  $\text{TiO}_2$  nanorod (TNR) arrays were synthesized and modified thermochemically under reductive conditions with an  $\text{H}_2$  stream at  $350^\circ\text{C}$  for  $2$  h [21,22]. As-synthesized TNR (Fig. S7) and hydrogen-treated TNR (h-TNR, Fig. 4a inset) samples showed similar rod structures  $\sim 1 \mu\text{m}$  in height and  $\sim 120$  nm in diameter. Despite this similar morphology, the latter was found to exhibit a significantly higher photoelectrochemical (PEC) performance (Fig. 4a) owing to the enhanced charge transfer in the oxygen vacancy-created  $\text{TiO}_2$ . The  $E_{\text{on}}$  values of TNR and h-TNR were similar at  $-0.4$  V, whereas the photocurrent ( $I_{\text{ph}}$ ) of h-TNR was  $\sim 40\%$  larger than that of TNR, reaching a plateau of  $\sim 2.2 \text{ mA cm}^{-2}$ . This value is close to the maximum  $I_{\text{ph}}$ , given the bandgap of rutile  $\text{TiO}_2$  ( $\sim 3.0$  eV). Notably, although the h-TNR was yellowish gray, there was no contribution of the visible-light absorption to the  $I_{\text{ph}}$  generation.

The PEC activity of the h-TNR electrode was further examined with regard to the oxidation of arsenite ( $\text{As(III)}$ ) to arsenate ( $\text{As(V)}$ ) at  $0.5$  and  $0.8$  V (Fig. 4b).  $\text{As(III)}$  is a representative aquatic pollutant, and its toxicity significantly decreases upon oxidation to  $\text{As(V)}$  [23,34,35]. The voltammogram of h-TNR with  $\text{As(III)}$  was found to be similar to that without  $\text{As(III)}$  (Fig. S8), indicating an insignificant interaction with the  $\text{TiO}_2$  surface and hence a minor pathway of direct charge transfer between  $\text{TiO}_2$  and  $\text{As(III)}$  [31,35]. At  $E = 0.5$  V, a constant  $I_{\text{ph}}$  of  $\sim 0.9 \text{ mA cm}^{-2}$  was flowed over  $10$  h, while  $\text{As(V)}$  was produced linearly during the PEC period. The FE for  $\text{As(V)}$  production was estimated to be  $> 80\%$ . When  $E$  increased to  $0.8$  V, an  $I_{\text{ph}}$  of  $\sim 1.7 \text{ mA cm}^{-2}$  was obtained, and the production of  $\text{As(V)}$  was enhanced, with an FE of  $> 90\%$ . These high FEs, particularly at the latter  $E$ , indicate that the photogenerated hole transfer to  $\text{As(III)}$  is efficient, whereas the competitive water oxidation is inhibited.

### 3.3. Sunlight-driven arsenite oxidation and simultaneous $\text{H}_2\text{O}_2$ production

We designed a two-compartment reactor separated by a proton-exchange membrane (PEM) to drive the PEC  $\text{As(III)}$  oxidation and the

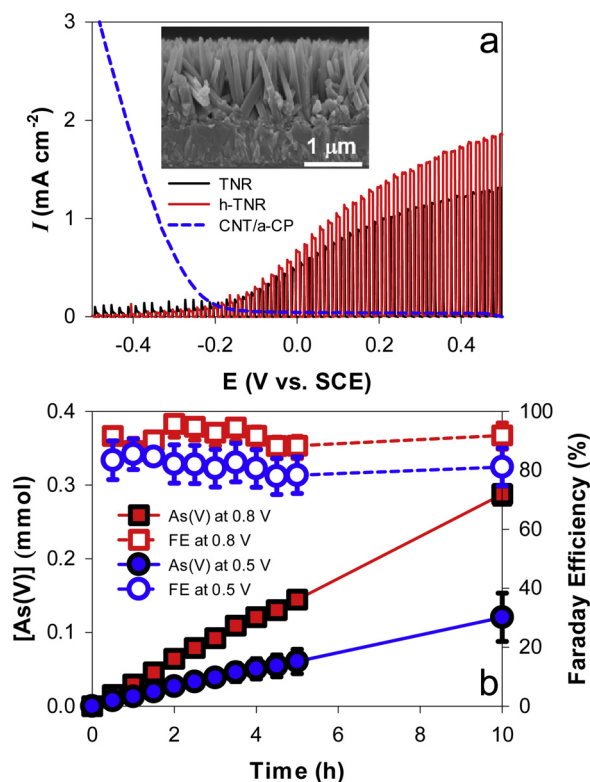


**Fig. 4.** (a) Chopped linear sweep voltammograms (LSVs) of TNR and h-TNR photoelectrodes immersed in aqueous sodium sulfate (0.1 M) containing As(III) (1 mM) under irradiation of AM 1.5 ( $100 \text{ mW cm}^{-2}$ ). The LSV of CNT/a-CP are also shown, for comparison. The inset shows a cross-sectional SEM image of hydrogen-treated TNR (h-TNR) arrays. (b) Photoelectrochemical production of As(V) using h-TNR electrodes held at 0.5 and 0.8 V vs. SCE in an aqueous sodium sulfate solution (0.1 M) containing 1 mM As(III). The Faradaic efficiencies for As(V) production are shown as well.

simultaneous  $\text{H}_2\text{O}_2$  production using h-TNR and CNT/a-CP couples. As a preliminary test, h-TNR was held at 0.5 V (i.e., vs. SCE) and irradiated with AM 1.5 light while  $\text{O}_2$  was bubbled through the solution in the CNT/a-CP compartment. A nearly constant  $I_{\text{ph}}$  of  $\sim 1 \text{ mA cm}^{-2}$  flowed, and the amounts of As(V) increased linearly with time, leading to an FE of  $> 80\%$  (Fig. S9). However, the  $\text{H}_2\text{O}_2$  production was disappointingly low, particularly in the initial stage (FE  $\sim 20\%$ ), and reached a plateau. This behavior was not observed when CNT/a-CP was tested as a half-electrode (see Fig. 3). The TNR and CNT/a-CP couple showed the same behavior (Fig. S9), suggesting that the physicochemical property of  $\text{TiO}_2$  was not the cause. We noted the low amount of  $\text{H}_2\text{O}_2$ , particularly in the initial stage, and suspected the intervention of photons. Although the thick  $\text{TiO}_2$  (both TNR and h-TNR) effectively absorbs most of the UV photons with energy greater than 3.1 eV ( $\sim 400 \text{ nm}$ ), a fraction of photons can be transmitted through the semi-transparent  $\text{TiO}_2$  and transparent PEM, leading to UV-induced decomposition of  $\text{H}_2\text{O}_2$ . To examine this possibility, two additional experiments were performed. First, the electrochemical HPR was conducted with CNT/a-CP in the conventional three-electrode configuration, while the solution was irradiated with AM 1.5 light. At E of  $-0.63 \text{ V}$ ,  $I$  of  $\sim 4.5 \text{ mA cm}^{-2}$  flowed; however, the FE was  $< 5\%$  (Fig. S10), which is significantly lower than the value in Fig. 3. Second, CNT/a-CP was coupled to h-TNR in the two-compartment cell with the PEM, and then a non-transparent film was inserted in front of the PEM to block the passage of UV light to the solution with the CNT/a-CP (Fig. 5a). The condition was the same as those in Fig. S9, except for the UV-blocking film. While a slightly larger  $I_{\text{ph}}$  of  $\sim 1.4 \text{ mA cm}^{-2}$  flowed, As(V) and  $\text{H}_2\text{O}_2$  were produced linearly with time in the absence of sign of a plateau. Their FEs were estimated to be  $\sim 80$  and  $100\%$ , respectively. These two experiments verify the

UV-induced decomposition of the  $\text{H}_2\text{O}_2$  produced in the CNT/a-CP compartment. As a result, the inhibition of the UV effect increased the FE of  $\text{H}_2\text{O}_2$  to  $\sim 100\%$ .

For practical operation, we attempted to use a DC power supply for the hybrid cell. Comparison of the LSVs of h-TNR and CNT/a-CP (Fig. 4a) suggested that a minimum DC voltage ( $E_{\text{DC}}$ ) of  $0.5 \text{ V}_{\text{DC}}$  is required for  $I_{\text{ph}}$  of  $\sim 1 \text{ mA cm}^{-2}$ . Considering the transient current in the LSVs, a voltage of  $0.7 \text{ V}_{\text{DC}}$  was applied to h-TNR and CNT/a-CP as an anode and cathode couple that were separated by a PEM. As shown in Fig. 5b,  $I_{\text{ph}}$  decreased slightly to  $\sim 1 \text{ mA cm}^{-2}$  in 1 h and reached a stable value of  $\sim 0.9 \text{ mA cm}^{-2}$  in 10 h. The applied DC voltage ( $0.7 \text{ V}_{\text{DC}}$ ) caused the anode and cathode to be biased by  $+0.4$  and  $-0.3 \text{ V}$  with respect to the solution (i.e., vs. SCE) over 10 h. The products in both compartments were analyzed (Fig. 5c); As(V) and  $\text{H}_2\text{O}_2$  were produced linearly with time. Their respective FEs of  $> 80$  and  $> 90\%$  were invariable with time and nearly the same as those obtained in the half-electrode systems (Figs. 3 and 4).

Although the h-TNR electrodes exhibited promising catalytic activity for As(III) oxidation, the intrinsic properties of  $\text{TiO}_2$  (e.g., wide bandgap, insufficient flatband potential, and small photocurrent) inevitably require an additional potential bias (e.g.,  $0.7 \text{ V}_{\text{DC}}$ ) for driving the anodic and cathodic reactions. To address this while achieving standalone, off-grid operation, a low-cost monocrystalline PV cell of  $0.1 \text{ cm}^2$  (only one tenth the size of h-TNR) was coupled to the PEC pair (h-TNR anode and CNT/a-CP cathode) (Fig. 5d). The employed PV cell showed a short-circuit current of  $\sim 3.2 \text{ mA}$  (i.e.,  $32 \text{ mA cm}^{-2}$ ) and an open-circuit voltage of  $\sim 0.8 \text{ V}$ , leading to a power-conversion efficiency of  $\sim 18.5\%$  (fill factor of  $\sim 0.78$ ). The two  $I$ - $V$  curves of the PV cell and the PEC pair coincided at  $I \sim 2 \text{ mA}$  and  $E \sim 0.7 \text{ V}$ , where the PV-PEC systems operated over 5 h. During this period, h-TNR and CNT/a-CP were biased at  $+0.4$  and  $-0.35 \text{ V}$ , respectively (Fig. 5d inset), while the As(V) and  $\text{H}_2\text{O}_2$  production continued at the rate of  $\sim 30 \mu\text{mol h}^{-1}$ . This production rate was twofold the DC power application ( $0.7 \text{ V}_{\text{DC}}$ ) (Fig. 5c), indicating that the  $I_{\text{ph}}$  of h-TNR was nearly maintained at  $\sim 1.8 \text{ mA cm}^{-2}$  during the PV-PEC process. Accordingly, the overall photoconversion energy efficiency was estimated to be  $\sim 1\%$ . Although the device efficiency of PV-PEC was low compared with the state-of-the-art PV-coupled electrocatalytic water splitting, the primary merit of this system is easy achievement of two important reactions in a single device at the maximum efficiency of photocatalysis (i.e.,  $\sim 1\%$  for  $\text{TiO}_2$  with a bandgap of 3–3.2 eV) with the assistance of a low-cost PV that is only one-tenth the size of the photocatalyst.

#### 4. Conclusions

Electrocatalytic  $\text{H}_2\text{O}_2$  production using CNT-loaded carbon papers driven by  $\text{TiO}_2$  nanorod array photoanodes that efficiently photocatalyze As(III) oxidation to As(V) in a two-compartment reactor was successfully demonstrated. The loading of CNT into acid-treated CPs enhanced the 2e-transfer process, increasing the  $\text{H}_2\text{O}_2$  selectivity and thereby leading to an FE of  $100\%$  for  $\text{H}_2\text{O}_2$  production from purged  $\text{O}_2$ . In the CNT/a-CP double-layer configuration, the acid treatment removed surface carbons and enhanced the electrical conductivity, whereas the CNT created a more porous structure, accelerating the solid/liquid/gas interfacial reaction. As a photoanode, h-TNR arrays exhibited enhanced photocurrents compared with TNR arrays owing to the improved conductivity, leading to an FE of  $> 80\%$  for the oxidation of As(III) to As(V). The high FEs for the anodic and cathodic reactions were maintained upon application of a DC voltage when both electrodes were placed in different compartments and UV-induced decomposition of  $\text{H}_2\text{O}_2$  was avoided. Finally, the overall process was operated with a commercial PV. Considering that most (photo)electrocatalytic processes are single-purpose—for either the production of renewable chemicals or the treatment of contaminated water under electric biases—the proposed off-grid, standalone hybrid PEC energy-water nexus process introduces a new research direction with great applicability.

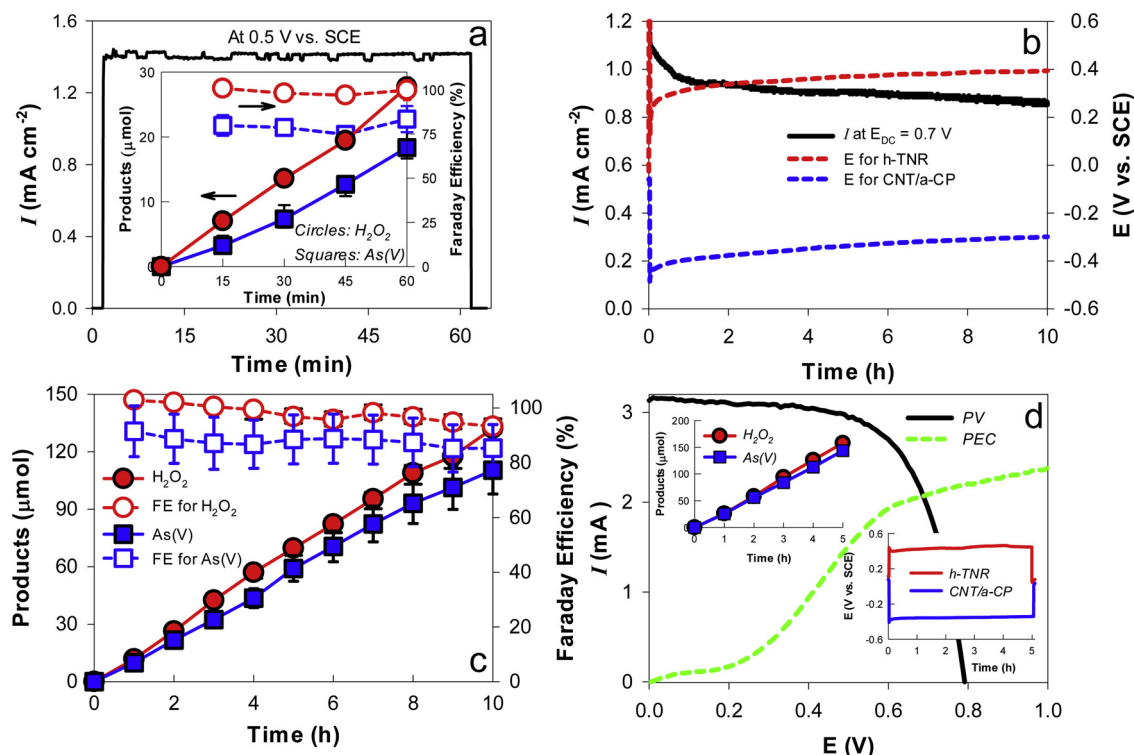


**Fig. 5.** (a–c) Photoelectrochemical As(III) oxidation and simultaneous H<sub>2</sub>O<sub>2</sub> production using the h-TNR photoanode and CNT/a-CP cathode in a two-compartment reactor (separated by a PEM) containing aqueous sodium sulfate (0.1 M). O<sub>2</sub> was purged through the catholyte only, while the anolyte was equilibrated with air. A non-transparent film was placed in front of the PEM to block the passage of UV light to the solution with the CNT/a-CP. In (a), h-TNR was held at +0.5 V vs. SCE (placed in the same compartment as the h-TNR). Inset: production of As(V) and H<sub>2</sub>O<sub>2</sub> in the h-TNR and CNT/a-CP compartments, respectively. In (b), a DC voltage of 0.7 V was applied to h-TNR with respect to the CNT/a-CP pair, and the currents of the pair were recorded. Additionally, each potential biased to h-TNR and CNT/a-CP was measured with respect to an SCE. Under this condition ( $E_{DC}$  of 0.7 V), the production of As(V) and H<sub>2</sub>O<sub>2</sub>, as well as their Faradaic efficiencies, are shown in (c). (d) I–V curves of an employed PV array (area of 0.1 cm<sup>2</sup>) and a PEC pair (h-TNR and CNT/a-CP; each 1 cm<sup>2</sup>). After the PV and PEC pair was coupled, the production of As(V) and H<sub>2</sub>O<sub>2</sub> was monitored, while each potential of the PEC pair was recorded with respect to the SCE.

## Acknowledgements

This research was supported by the Basic Science Research Program (2019R1A2C2002602 and 2018R1A6A1A03024962), the Framework of International Cooperation Program (NRF-2018K2A9A1A01090462), and the Global Research Laboratory (GRL) Program (2014K1A1A2041044) through the National Research Foundation, Korea. In addition, we are grateful for the financial support provided by the Korea CCS R&D Center (KCRC) (no. 2014M1A8A1049354). This publication was made possible by a grant from the Qatar National Research Fund under its National Priorities Research Program (NPRP 10-1210-160019).

## Appendix A. Supplementary data

Supplementary material related to this article can be found, in the online version, at doi:<https://doi.org/10.1016/j.apcatb.2019.03.060>.

## References

- J. Garcia-Serna, T. Moreno, P. Biasi, M.J. Cocero, J.P. Mikkola, T.O. Salmi, Engineering in direct synthesis of hydrogen peroxide: targets, reactors and guidelines for operational conditions, *Green Chem.* 16 (2014) 2320–2343.
- The Global Hydrogen Peroxide Market, Hydrogen Peroxide Market Trends, Global Industry Analysts, Inc, 2016.
- C. Samanta, Direct synthesis of hydrogen peroxide from hydrogen and oxygen: an overview of recent developments in the process, *Appl. Catal. A* 350 (2008) 133–149.
- J.M. Campos-Martin, G. Blanco-Brieva, J.L.G. Fierro, Hydrogen peroxide synthesis: an outlook beyond the anthraquinone process, *Angew. Chem. Int. Ed.* 45 (2006) 6962–6984.
- D. Hancu, J. Green, E.J. Beckman, H<sub>2</sub>O<sub>2</sub> in CO<sub>2</sub>/H<sub>2</sub>O biphasic systems: green synthesis and epoxidation reactions, *Ind. Chem. Eng. Res.* 41 (2002) 4466–4474.
- I. Katsounaros, W.B. Schneider, J.C. Meier, U. Benedikt, P.U. Biedermann, A.A. Auer, K.J.J. Mayrhofer, Hydrogen peroxide electrochemistry on platinum: towards understanding the oxygen reduction reaction mechanism, *Phys. Chem. Chem. Phys.* 14 (2012) 7384–7391.
- T. Kondo, C.L. Song, N. Hayashi, T. Sakurai, M. Shibata, H. Notsu, I. Yagi, Electrocatalytic activity for oxygen reduction reaction of pseudomorphic Pt monolayer prepared electrochemically on a Au(111) surface, *Chem. Lett.* 40 (2011) 1235–1237.
- S.Y. Yang, H.W. Jeong, B.-j. Kim, D.S. Han, W. Choi, H. Park, Electrocatalytic co-generation of reactive oxygen species for synergistic water treatment, *Chem. Eng. J.* 358 (2019) 497–503.
- N.C.D. Nath, S.Y. Choi, H.W. Jeong, J.J. Lee, H. Park, Stand-alone photoconversion of carbon dioxide on copper oxide wire arrays powered by tungsten trioxide/dye-sensitized solar cell dual absorbers, *Nano Energy* 25 (2016) 51–59.
- M.S. Prevot, K. Sivula, Photoelectrochemical tandem cells for solar water splitting, *J. Phys. Chem. C* 117 (2013) 17879–17893.
- J. Brillet, J.H. Yum, M. Cornuz, T. Hisatomi, R. Solarska, J. Augustynski, M. Graetzel, K. Sivula, Highly efficient water splitting by a dual-absorber tandem cell, *Nat. Photonics* 6 (2012) 823–827.
- G.-h. Moon, W. Kim, A.D. Bokare, N. Sung, W. Choi, Solar production of H<sub>2</sub>O<sub>2</sub> on reduced graphene oxide–TiO<sub>2</sub> hybrid photocatalysts consisting of earth-abundant elements only, *Energy Environ. Sci.* 7 (2014) 4023–4028.
- S.N. Li, G.H. Dong, R. Hailili, L.P. Yang, Y.X. Li, F. Wang, Y.B. Zeng, C.Y. Wang, Effective photocatalytic H<sub>2</sub>O<sub>2</sub> production under visible light irradiation at g-C<sub>3</sub>N<sub>4</sub> modulated by carbon vacancies, *Appl. Catal. B* 190 (2016) 26–35.
- X. Zong, H.J. Chen, B. Seger, T. Pedersen, M.S. Dargusch, E.W. McFarland, C. Li, L.Z. Wang, Selective production of hydrogen peroxide and oxidation of hydrogen sulfide in an unbiased solar photoelectrochemical cell, *Energy Environ. Sci.* 7 (2014) 3347–3351.
- J.J. Zhang, X.X. Chang, Z.B. Luo, T. Wang, J.L. Gong, A highly efficient photoelectrochemical H<sub>2</sub>O<sub>2</sub> production reaction with Co<sub>3</sub>O<sub>4</sub> as a co-catalyst, *Chem. Commun.* 54 (2018) 7026–7029.
- X.M. Yu, M.H. Zhou, G.B. Ren, L. Ma, A novel dual gas diffusion electrodes system for efficient hydrogen peroxide generation used in electro-Fenton, *Chem. Eng. J.* 263 (2015) 92–100.
- M. Panizza, G. Cerisola, Electrochemical generation of H<sub>2</sub>O<sub>2</sub> in low ionic strength media on gas diffusion cathode fed with air, *Electrochim. Acta* 54 (2008) 876–878.
- C.H. Choi, H.C. Kwon, S. Yook, H. Shin, H. Kim, M. Choi, Hydrogen peroxide

- synthesis via enhanced two-electron oxygen reduction pathway on carbon-coated Pt surface, *J. Phys. Chem. C* 118 (2014) 30063–30070.
- [19] E. Sadeghi, N. Djilali, M. Bahrami, Effective thermal conductivity and thermal contact resistance of gas diffusion layers in proton exchange membrane fuel cells. Part 1: effect of compressive load, *J. Power Source* 196 (2011) 246–254.
  - [20] E. Brillas, I. Sires, M.A. Oturan, Electro-Fenton process and related electrochemical technologies based on Fenton's reaction chemistry, *Chem. Rev.* 109 (2009) 6570–6631.
  - [21] H.W. Jeong, K.J. Park, D.S. Han, H. Park, High efficiency solar chemical conversion using electrochemically disordered titania nanotube arrays transplanted onto transparent conductive oxide electrodes, *Appl. Catal. B* 226 (2018) 194–201.
  - [22] S. Kim, G. Piao, D.S. Han, H.K. Shon, H. Park, Solar desalination coupled with water remediation and molecular hydrogen production: a novel solar water-energy nexus, *Energy Environ. Sci.* 11 (2018) 344–353.
  - [23] K. Christen, The arsenic threat worsens, *Environ. Sci. Technol.* 35 (2001) 286A–291A.
  - [24] Y.K. Kim, H. Park, Light-harvesting multi-walled carbon nanotubes and CdS hybrids: application to photocatalytic hydrogen production from water, *Energy Environ. Sci.* 4 (2011) 685–694.
  - [25] Y.K. Kim, H. Park, How and to what extent do carbon materials catalyze solar hydrogen production from water? *Appl. Catal. B* 125 (2012) 530–537.
  - [26] R.D.C. Soltani, A. Rezaee, A.R. Khataee, H. Godini, Electrochemical generation of hydrogen peroxide using carbon black-, carbon nanotube-, and carbon black/carbon nanotube-coated gas-diffusion cathodes: effect of operational parameters and decolorization study, *Res. Chem. Intermed.* 39 (2013) 4277–4286.
  - [27] K. Kosaka, H. Yamada, S. Matsui, S. Echigo, K. Shishida, Comparison among the methods for hydrogen peroxide measurements to evaluate advanced oxidation processes: application of a spectrophotometric method using copper(II) ion and 2,9-dimethyl-1,10-phenanthroline, *Environ. Sci. Technol.* 32 (1998) 3821–3824.
  - [28] M.J. Park, S.J. Kwon, H.S. Park, S.J. Yoo, J.H. Jang, H.J. Kim, S.W. Nam, J.Y. Kim, Urchin-shaped hollow iron-nitrogen-doped carbon microspheres as high-performance electrocatalysts for oxygen reduction, *J. Electrochem. Soc.* 164 (2017) F224–F228.
  - [29] M.J. Park, J.H. Lee, K.P.S.S. Hembram, K.R. Lee, S.S. Han, C.W. Yoon, S.W. Nam, J.Y. Kim, Oxygen reduction electrocatalysts based on coupled iron nitride nanoparticles with nitrogen-doped carbon, *Catalysts* 6 (2016).
  - [30] V. Lenoble, V. Deluchat, B. Serpaud, J.C. Bollinger, Arsenite oxidation and arsenate determination by the molybdene blue method, *Talanta* 61 (2003) 267–276.
  - [31] J. Kim, D. Kwon, K. Kim, M.R. Hoffmann, Electrochemical production of hydrogen coupled with the oxidation of arsenite, *Environ. Sci. Technol.* 48 (2014) 2059–2066.
  - [32] Y.K. Kim, S.K. Lim, H. Park, M.R. Hoffmann, S. Kim, Trilayer CdS/carbon nanofiber (CNF) mat/Pt-TiO<sub>2</sub> composite structures for solar hydrogen production: effects of CNF mat thickness, *Appl. Catal. B* 196 (2016) 216–222.
  - [33] A. Dobrzynska, A.R. Zeradjanin, J. Masa, M. Blicharska, D. Wintrich, P.J. Kulesza, W. Schuhmann, Evaluation of kinetic constants on porous, non-noble catalyst layers for oxygen reduction—a comparative study between SECM and hydrodynamic methods, *Catal. Today* 262 (2016) 74–81.
  - [34] P.A. O'Day, D. Vlassopoulos, X. Meng, L.G. Benning, Advances in arsenic research: integration of experimental and observational studies and implications for mitigation, *Am. Chem. Soc.* (2005).
  - [35] H. Lee, W. Choi, Photocatalytic oxidation of arsenite in TiO<sub>2</sub> suspension: kinetics and mechanisms, *Environ. Sci. Technol.* 36 (2002) 3872–3878.